AIAA JOURNAL
Vol. 32, No. 11, November 1994

Multiple Degree-of-Freedom Force-State Component Identification

Brett P. Masters* and Edward F. Crawley†
Massachusetts Institute of Technology, Cambridge, Massachusetts 02139

Force-state mapping is extended to allow the quasistatic characterization of realistic multiple degree-of-freedom systems whose constitutive relations are nonlinear, dissipative, coupled, and depend on memory of past states. A general constitutive force-state model is formulated, which includes dynamic hysteresis phenomena typical of that found in deployable structures. A two step parameter identification approach is developed, which employs a linear extended least squares and a nonlinear least squares fit. A six degree-of-freedom force-state testing device was constructed and used to obtain data on one bay of a simple truss and on one bay of the mid-deck 0-gravity dynamics experiment deployable truss.

Introduction

HIGH performance prediction of open- and closed-loop structural response requires an accurate model of the structure, including potentially nonlinear joints and mechanisms. Typically, a structural model evolves through three stages, beginning with a first generation model derived from design drawings and handbook material data. This model is available early in the design cycle, but its accuracy is limited by poor modeling (due to inexact elements, arbitrary simplifications, etc.), mismodeling (due to human error), and nonmodeling (of effects such as nonlinearities and dissipation).

A second generation of the model is formed by updating the original model with measurements made on structural components. Such measurements are commonly used to update the mass and stiffness terms. However, within the state of the art, it is difficult to predict nonlinear and dissipative behavior based on component measurements. Third generation models incorporate information derived from dynamic modal testing data. Full vehicle dynamic ground testing is not always possible and, when conducted, yields data corrupted by gravity and suspension effects.[3,10] In flight, testing provides the most reliable model but usually very late in the development program.

There is clearly a need to improve the process of component testing for the purposes of model updating. Three approaches are under development: substructural modal testing, multiple boundary condition testing, and force-state mapping. Substructural modal testing is most valuable when the modes of a substructure are in the same frequency range as the modes of the full structure.[9] Multiple boundary condition modal testing also obtains dynamic information but at elevated frequencies and with artificial boundary conditions. Both techniques rely on the linearity of the structure when extrapolating the results. Force-state mapping, in which the weakly nonlinear behavior of a component is measured quasistatically, can be used with nonlinear and dissipative structures but to date has been limited to single degree-of-freedom systems.[1]

The objective of this work is to extend force-state mapping to the characterization of realistic multiple degree-of-freedom (DOF) systems whose constitutive relations are nonlinear, dissipative, coupled, and depend on memory of past states. The procedure will produce the identified component information necessary for eventual use in updating second generation structural dynamic models.

Research on model updating is motivated by the results for the structural test article (STA) of the mid-deck 0-gravity dynamics experiment (MODE).[7] Open-loop dynamics testing of the STA was performed both on-orbit (on STS-48) and in the laboratory. The STA is an engineering scale model which consists of sections of wire-braced deployable bays, linked in several configurations by erectable bays and/or a one bay rotary joint. In one of the deployable sections an adjustable pretension bay was incorporated with three possible joint preload settings in the bracing wires.

The measured differences in the STA zero- and one-gravity linear and nonlinear behavior are quite striking. On average the data show softening in resonance frequency of 1% and increased damping of 0.5% in zero-gravity relative to one-gravity tests.[6] The data in both zero and one-gravity show weak to moderate nonlinear response characteristics as a function of input force amplitude, with the nonlinearity causing softening and dampening with increased force, decreased preload, and reduction in gravity level.

The models of the MODE STA which existed prior to flight were typical of first generation, undamped linear finite element models. Of course, they failed to predict damping, changes in damping, changes in frequency, and nonlinear behavior. A modeling process which captures the linear effects of gravity stiffening and suspension is now available,[10] but a process to characterize the damping and nonlinear behavior and to obtain data for second generation model updates must be developed.

Traditionally, the modeling of local nonlinearities (such as joints) has been approached using load-stroke test information. Transmitted force that depends explicitly on velocity or on true memory effects can only be incompletely inferred from static force-displacement measurements alone. This deficiency is addressed by quasistatic force-state mapping. Single degree-of-freedom force-state mapping of systems without memory has been developed for simple joints[1,2] and applied to joints such as those incorporated in Langley Research Center's Mini Mast.[12]

In single degree-of-freedom force-state mapping the force transmitted through the joint is represented as a function of the displacement and velocity across the joint. Experimentally, the approach requires the measurement or estimation of force, acceleration, displacement, and velocity. The measured force is corrected for the inertia force, and conceptually plotted vs the displacement and velocity states of the system to produce the force-state map. Figure 1 shows a representative map of a deadband spring with coulomb friction (note the change in force as the velocity changes sign). If the joint dynamics are sufficiently high in frequency, then quasistatic testing can be performed without the explicit inertia correction.

Single DOF force-state mapping serves as a foundation for the multiple DOF problem. However, the single DOF model does not address how the force transmission characteristics are modified by loads in other directions. When a number of potentially nonlinear elements are built up into a bay unit, the interaction of load in multiple directions, coupled with the geometrical arrangement of elements, may lead to conglomerate effects not otherwise captured in single DOF analysis.

Received June 19, 1993; revision received May 31, 1994; accepted for publication May 31, 1994.

*Graduate Research Assistant, Space Engineering Research Center.
†Professor of Aeronautics and Astronautics, Space Engineering Research Center.

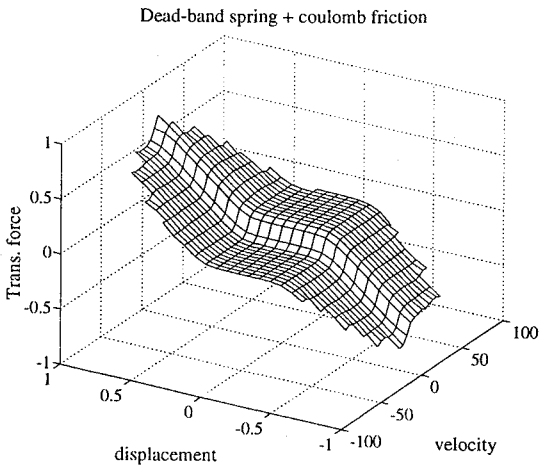

Fig. 1 Representative single degree-of-freedom force-state maps.

The approach taken in this work is to characterize an entire bay of the truss structure undergoing shear, bending, extension, and twisting as a 12 DOF beam element. Eventually, the identified parameters of the bay will be used to predict the weakly nonlinear response of the MODE truss using numerical methods such as time integration.[8] However, such prediction and correlation with the MODE modal data is beyond the scope of the current paper.

The next section describes the extension of the force-state methodology to multiple degrees of freedom and the inclusion of memory effects. The methodology consists of two parts: first, the analytical formulation of the nonlinear structural constitutive equations, whose parameters will be identified; second, the process of extracting the parameters from the data. In the proposed process, a two step procedure is used: first, a static extended least squares process to identify linear parameters and evaluate experimental precision; second, a continuation algorithm to solve a nonlinear least squares problem and fit the model constitutive relations to the data.

This methodology requires an experimental apparatus to obtain the multiple DOF force-state range. A six DOF dynamic testing machine was constructed using six shakers in a Stuart platform arrangement. Six measurements of force and moment are made at each of the two ends of the test bay. Six measurements of displacement and rotation are made simultaneously, while the bay is exercised in all six generalized directions about its unconstrained end. The device and data reduction will be described in the third section.

The characteristics of two tested truss bays are identified using the force-state tester. One is a nominally linear reference or calibration bay. The second is the adjustable deployable bay of the MODE hardware. The identified parameters are checked for internal consistency and against linear models as appropriate. They reveal a fundamental dynamic hysteresis effect present in the joints of the MODE hardware.

Multiple Degree-of-Freedom Force-State Identification

General Force-State Model

To extract multiple degree of freedom structural component constitutive parameters, an extension of single DOF force-state mapping is required. The extension expands the single DOF analysis to include the coupling effects of a multidegree-of-freedom system. In the extended analysis, memory effects are also incorporated. As with the single DOF analysis, small deflections have been assumed so as to capture the localized nonlinearities of a component about a desired operation point and to eliminate any nonlinearity in the inertia tensor.

Equation (1) describes the general form of the force transmitted by the component.

$$F_{Ti} = F_{1D}(x_i, \dot{x}_i) + F_{1ND}(x_j, \dot{x}_j)_{j\neq i} + F_{2D}\left(x_i^2, x_i\dot{x}_i, \dot{x}_i^2\right) + F_{2ND}(x_ix_j, x_i\dot{x}_j, \dot{x}_i\dot{x}_j)_{j\neq i} + F_{3D}\left(x_i^3, x_i^2\dot{x}_i, x_i\dot{x}_i^2, \dot{x}_i^3\right) + F_{3ND}(x_ix_jx_k, x_ix_j\dot{x}_k, x_i\dot{x}_j\dot{x}_k, \dot{x}_i\dot{x}_j\dot{x}_k)_{j,k\neq i} + F_{DNA}(x_i, \dot{x}_i) + [\text{NDNA}] + F_{DM}(x_i, \dot{x}_i) + [\text{NDM}] + [\text{HOT}] \quad (1)$$

F_{Ti} is the ith generalized transmitted force through the component. F_{1D}, F_{2D}, and F_{3D} represent first-, second-, and third-order diagonal dependencies of the generalized force on the generalized displacements. F_{DNA} similarly represents diagonal nonanalytic dependencies such as deadbands, material damping, and coulomb friction. These terms were present in the previously developed single DOF force-state characterization.[1] Appended is the term F_{DM} describing diagonal memory. F_{DM} describes the conditional dependence of the ith transmitted force on the history of the ith DOF and its rate. The added terms F_{1ND}, F_{2ND}, and F_{3ND} describe the nondiagonal coupling of the ith generalized force to the jth degree of freedom in analytic form to third order. Nondiagonal nonanalytic (NONA), nondiagonal memory (NDM), and higher order analytic terms (HOT) could be added to completely generalize the formulation.

F_{Ti} is the structural force operator and excludes the inertia operator. If the dynamic displacements are small, then the component inertia can be computed and subtracted from the total transmitted force to yield the net structural force of Eq. (1). Alternatively, quasi-static identification can be performed. If the dynamic displacements are large, then care must be taken to compute or possibly identify a nonlinear inertia matrix.

Reduced Force-State Model

In practice, Eq. (1) must be specialized to contain the terms of physical significance for a specific application. Multidegree-of-freedom component parameter identification for MODE is approached by modeling one truss bay as a general 12 DOF cantilevered beam element. The parameters of the six DOF constitutive relations describing the unconstrained end are identified by representing the bay, which has many internal load paths, as a beam. Nonlinearities associated with the diagonal bracing wires, knee joints, and node mechanisms are smeared, as are the linear components, within an equivalent continuum model. This amounts to elimination of the bay internal DOF and will eventually limit the modal predictions of the MODE truss to that of the global modes occuring at frequencies below localized modes.

Reduction of the model of Eq. (1) is obtained by making two assumptions, both consistent with the data: the component is only weakly nonlinear and the majority of the strain energy is stored in the diagonal stiffness elements. A consequence of the first assumption is that higher order time derivatives can be neglected (those in $\dot{x}^2$, $\dot{x}^3$, etc.) along with quartic and higher order analytic terms. A consequence of the second assumption is that a less detailed parameterization of the nondiagonal elements of F_{Ti} is necessary.

The MODE specific force-state description is thus written as shown in Eqs. (2–6).

$$F_{T_i} = F_{D_i} + \sum_{j\neq i} F_{ND_{ij}} \quad (2)$$

$$F_{D_i} = K_{1_i}x_i + D_{1_i}\dot{x}_i + K_{2_i}x_i^2 + K_{3_i}x_i^3 + F_{M_i}(x_i, \dot{x}_i) = F_{ii} \quad (3)$$

$$F_{ND_{ij}} = \left[K_{1_{ij}}x_j + D_{1_{ij}}\dot{x}_j + K_{2_{ij}}x_j^2 + K_{3_{ij}}x_j^3\right]_{j\neq i} = (F_{ij})_{j\neq i} \quad (4)$$

$$f_{T_i} = F_{T_i} + e_i \quad (5)$$

The modeled structural force component F_{T_i} is separated into diagonal and nondiagonal contributions. The diagonal functions F_{D_i} are represented by cubic stiffness polynomials, linear damping, and memory terms as shown in Eq. (3). The nondiagonal contributions $F_{ND_{ij}}$ are represented as cubic stiffness polynomials and linear damping terms. Contributions to the stiffness and dissipation from higher order tensors are projected onto decoupled DOF space in such a way as to minimize the error e_i between the model F_{T_i} and the data f_{T_i}.

Inspection of the MODE data motivates the modeling of the nonlinear memory, $F_{M_i}(x_i, \dot{x}_i)$. The data presented by Crawley et al.[7] suggest softening and dampening with increased amplitude, consistent with mechanical hysteresis postulated by Prandtl[14] and cited in Ref. 13.

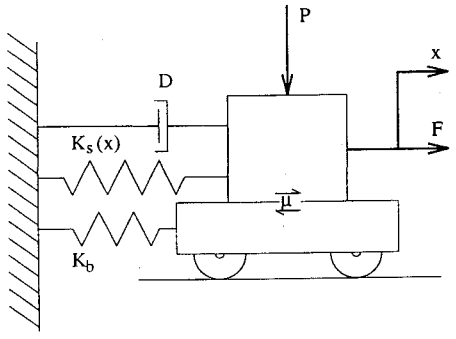

Fig. 2 Single slip dynamic hysteresis model.

A schematic of the hysteresis model is shown in Fig. 2. The model represents dynamic hysteresis as a sliding massless block in frictional contact with an elastically constrained massless cart. The two parameters, normal load P and friction coefficient μ are reduced to a slip force F_s, which represents the force across the block/cart interface that initiates joint slip. Also shown in Fig. 2 are K_s and D which represent the cubic stiffness polynomial and the linear damping term of Eq. (3) respectively.

Equation (6) is based on the physics of Fig. 2, which is extended to model multiple slip dynamic hysteresis. The conditional nature of Eq. (6) is typical of a bay containing many slip interfaces which stick and slip again after a change in the sense of direction.

$$F_M(x,\dot{x}) = \begin{cases} -K_b x & |K_b x| < |F_s| \quad \delta_n < \delta_c \\ -C_3\xi^3 - C_2\xi^2 - C_1\xi + F_s & x > -\delta_c \quad \dot{x} < 0 \\ F_s & x < -\delta_c \quad \dot{x} < 0 \\ C_3\xi^3 + C_2\xi^2 + C_1\xi - F_s & x < \delta_c \quad \dot{x} > 0 \\ -F_s & x > \delta_c \quad \dot{x} > 0 \end{cases} \tag{6}$$

$$\delta_c = F_s/K_b \tag{7}$$

$$\delta_n = |x| \qquad \text{when } \dot{x} \text{ changes sign} \tag{8}$$

$$C_1 = K_b \exp\left(-\frac{|\delta_n - \delta_c|}{\delta_c}\right) \tag{9}$$

$$C_2 = \frac{6F_s - K_b(\delta_n + \delta_c)}{(\delta_n + \delta_c)^2} - \frac{2C_1}{(\delta_n + \delta_c)} \tag{10}$$

$$C_3 = \frac{-4F_s + K_b(\delta_n + \delta_c)}{(\delta_n + \delta_c)^3} + \frac{C_1}{(\delta_n + \delta_c)^2} \tag{11}$$

$$\xi = |x - \text{sign}(\dot{x})\delta_c| \tag{12}$$

The slipforce F_s is the generalization of the total slipforce required to slip all joints in the prescribed motion, δ_c is the generalized slip deflection, and δ_n is the memory parameter. Just after all sliding joints within the component have been brought to rest and the sense of direction changes sign, the force-deflection curve of F_M has slope of K_b. After the sense of direction changes sign, the individual friction surfaces progressively break into slip. As progressively more surfaces slip, the transmitted force component due to F_M relaxes to $-\text{sign}(\dot{x})F_s$. The process begins again at the next change in sense of direction. Smoothness of transition between conditions is determined by the cubic dependence and the exponential dependence of C_1. In general, a combination of the conditions on and smoothness of the relative motion ensures that the model obeys Prandtl's three laws.

Linear Parameter Identification

The problem of identifying the parameters of Eqs. (3) and (4) consists of three parts. First, find the best set of input forces to identify the chosen parameters in the presence of measurement noise. Second, obtain a linear least squares estimate for the linear parameters as an initial guess for a continuation algorithm. Third, use the continuation algorithm, which incorporates nonlinear least squares problems, to identify nonlinear constitutive parameters. With multiple degrees of freedom, the problem of choosing input forces separates into finding the best input time history and the best spatial input directions.

The selection of input time history is driven by the requirement to have enough information in the state hyperplane so as to allow functional fits of Eqs. (3) and (4), i.e., enough data must be recorded in the state space so that the multidimensional force-state map can be identified, densely, with no holes.[1] A sinusoid which is ramped from zero to a peak and then to zero was used for the results presented in this paper. The ramped sinusoid was asymmetric about the peak ramp amplitude so that the signal had no static component. The maximum amplitude of the input is determined by the goals of the experiment, which for the MODE bay was the range of expected dynamic loads.

Extension to multiple degrees of freedom allows the experiment designer to vary the input direction within the vectors of applied generalized forces. By either a single test during which the direction varies, or a series of tests each with a fixed direction, data must be obtained which span the input direction space. The best set of directions will depend on the arrangement of sensors, the sensor noise characteristics, and the degree of stiffness coupling in the component being identified. The approach suggested is to postulate several sets of directions to be used, test them, and evaluate the best directions by comparing the standard deviations of the parameters of interest, as described subsequently.

Once data are taken over the selected sets of directions, an extended least squares analysis is used to identify the linear parameters of the model fit to the data as well as the standard deviations of these parameters. Equations (13–17) are written for the six unconstrained DOF identification of linear compliance parameters. The equations are inherently recursive. A full time sequence of test data is divided into L time histories ($l = 1, 2, \ldots, L$) of sufficient number length, where n is the number of DOF (6), to identify the 36 compliance parameters. The recursive equations are

$$\begin{bmatrix} \tilde{\boldsymbol{x}}_l \\ \tilde{\boldsymbol{C}}_l \end{bmatrix} = F_l \tilde{\boldsymbol{C}}_{l+1} + \begin{bmatrix} \boldsymbol{e}_x \\ \boldsymbol{e}_c \end{bmatrix}$$

$$\boldsymbol{e}_x = \eta_x + \eta_f C_l + F_l \eta_{C_l}$$

$$\tilde{\boldsymbol{x}} = \begin{bmatrix} \boldsymbol{x}_1^T & \boldsymbol{x}_2^T \ldots \boldsymbol{x}_n^T & \tilde{\boldsymbol{C}}_l^T \end{bmatrix}^T \tag{13}$$

$$\tilde{\boldsymbol{C}} = \begin{bmatrix} C_{11} & C_{12} \ldots C_{16} & C_{21} \ldots C_{66} \end{bmatrix}^T$$

$$F_l = \begin{bmatrix} \boldsymbol{f}_1^T & \boldsymbol{0}_{[1\times 30]} \\ \vdots & \vdots \\ \boldsymbol{0}_{[1\times 30]} & \boldsymbol{f}_6^T \\ & I_{[36\times 36]} \end{bmatrix}$$

where $\tilde{\boldsymbol{x}}_l$ is a vector of n time measurements of the displacement DOF $\boldsymbol{x}$, augmented with the previous least squares solution of the compliance parameters $\boldsymbol{C}_l$, also arranged as a vector. F_l is a matrix of n measurements of input force, arranged as shown, augmented with the identity representing pseudomeasurement of the parameters. The error $[\boldsymbol{e}_x \quad \boldsymbol{e}_c]^T$ is assumed Gaussian, zero mean, with covariance Ψ. The vector $\boldsymbol{e}_x$ includes error in the displacement measurement, error in force measurement propagated through the last estimate of the compliance, and error in the compliance parameters multiplied by the next time increment of force. The vector $\boldsymbol{e}_C$ represents the underlying assumption of the extended least squares that the parameters are inherently uncertain. The recursive solution of Eq. (13) is shown in Eq. (14) with the corresponding update of the covariance matrix in Eq. (15).

$$\tilde{\boldsymbol{C}}_{l+1} = \left(F_l^T \Psi_l^{-1} F_l\right)^{-1} F_l^T \Psi_l^{-1} \begin{bmatrix} \tilde{\boldsymbol{x}}_l \\ \tilde{\boldsymbol{C}}_l \end{bmatrix} \tag{14}$$

$$\Psi_{C_{l+1}} = \left[F_{l+1}^T \Psi_l^{-1} F_{l+1}\right]^{-1} \tag{15}$$

The matrix Ψ is initialized with variance estimates Ψ_0, made from inspecting the time domain data. The results of the estimation process are the least squares solution to the compliance parameters and the covariance matrix Ψ. The covariance can be partitioned into those elements associated with the states and parameters,

$$\Psi = \begin{bmatrix} \psi_x & \psi_{xC} \\ \psi_{Cx} & \psi_C \end{bmatrix} \tag{16}$$

$$\sigma_C = \sqrt{\frac{\text{diag}(\psi_C)}{m - 36}} \tag{17}$$

where σ_C is the standard deviation of the estimated compliance parameters, m is the total number of measured data points used in the identification, and 36 is the total number of identified parameters. The σ_C can then be normalized by the identified parameters to produce a vector of normalized standard deviations for eventual comparison of the various sets of test directions. From these results, a choice of the best set of input directions is made based on the desired identifiable parameters. The input directions are then implemented by a careful calibration of the component tester as described in the experimental procedure section.

Nonlinear Parameter Identification

Having selected the input directions and time history, the general problem of identifying a nonlinear component can proceed. For the following development, k distinct test directions which span the input generalized displacement space are assumed. After the input output data are taken, the linear least squares can be used to establish an initial guess for the linear parameters. The nonlinear parameter estimation problem is approached by using nonlinear least squares fit. Function fits of the F_{ii} in Eq. (3) are computed using the Levenburg-Marquart nonlinear least squares algorithm,[4] whereas fits of the F_{ij} of Eq. (4) are computed using ordinary least squares. The function fits are performed by initializing the process, as shown by step 1, then iterating to convergence in step 2 using a continuation algorithm.

Step 1) Initialization:
for $i, k = 1, 6$ let

$$F_{ij} = 0 \qquad j \neq i$$

solve for F_{ii}

$$(f_{Ti})_k = F_{ii} + e_{ik}$$

Step 2) Iteration on an outer loop of k and inner loop of i: while $r = 0 \rightarrow 1$,
for $k = 1, 6$,
for $i = 1, 6$,
if $i = k$ solve for F_{ii}

$$(f_{Ti})_k = F_{ii} + r \sum_{j \neq i} F_{ij} + e_{ik}$$

else solve for F_{ik}

$$(f_{Ti})_k = F_{ii} + (F_{ij})_{j=k} + r \sum_{j \neq i,\, j \neq k} F_{ij} + e_{ik}$$

where the measurements are the $(f_{Ti})_k$ (the ith component of total force transmitted taken in the kth input direction) and the DOF $(x_j, \dot{x}_j)$ implicit in the F_{ii} and F_{ij} represented in Eqs. (3) and (4).

Step 1 initializes the process by solving for the diagonal functions, by iterating over the k distinct test directions while minimizing the error e_{ik}. No information can be used from the F_{ij} in this step as they are yet to be determined.

Step 2 requires multiple iterations to minimize the matrix of error e_{ik} while varying the continuation parameter r. The continuation parameter determines the weight on the previously identified nondiagonal row information, F_{ij} $j \neq i, k$, and varies from zero to one. This allows numerical conditioning of the algorithm. In this step, two successive loops are performed: the inner loop over the i force components and the outer loop over the k dominant input directions. The continuation algorithm initializes with the assumption that the F_{ij} are zero. The algorithm proceeds with identifying and eventually reidentifying the F_{ij} $(i, j = 1, 6)$ using parameter information from the preceding iteration. After the continuation parameter is set equal to one, further iterations are performed until a norm of the error matrix is reduced to a preset threshold.

The implemented algorithm involves subtraction and, therefore, is not robust to identifying parameters near the noise floor. Some combination of program control and user input is required to eliminate the possibility of errors made when fitting low level noise; i.e., identifying parameters that are nominally zero. By monitoring the fit convergence, the user also determines whether the model fit is either over or under specified.

Experimental Hardware and Test Procedures

Hardware

The hardware used in the experiment consists of a simple reference or calibration bay, an adjustable preload deployable bay of the MODE STA, and a unique six DOF force-state component tester. The functional requirements for the component tester are that it accommodate test specimens of MODE component size, and that it possess the following: six axes of independently controllable actuators, whose load and stroke capability exceed the maximum dynamic range seen by the MODE STA components; 12 channels of load sensors capable of measuring six reactions at each end of the bay, compatible with MODE STA loads; and six channels of deflection sensors, capable of measuring six generalized deflections at the unconstrained end of the bay, compatible with MODE deflections.

A detailed plan and elevation of the component tester is shown in Fig. 3. Six voice coil actuators are mounted between a 1-ton granite base and a stiffened aluminum plate in a Stuart platform arrangement. The granite base is air supported so that building disturbances above 2.5 Hz are isolated from the tester. Soft flexural bearings provide effective pivots at both ends of the load applying struts while

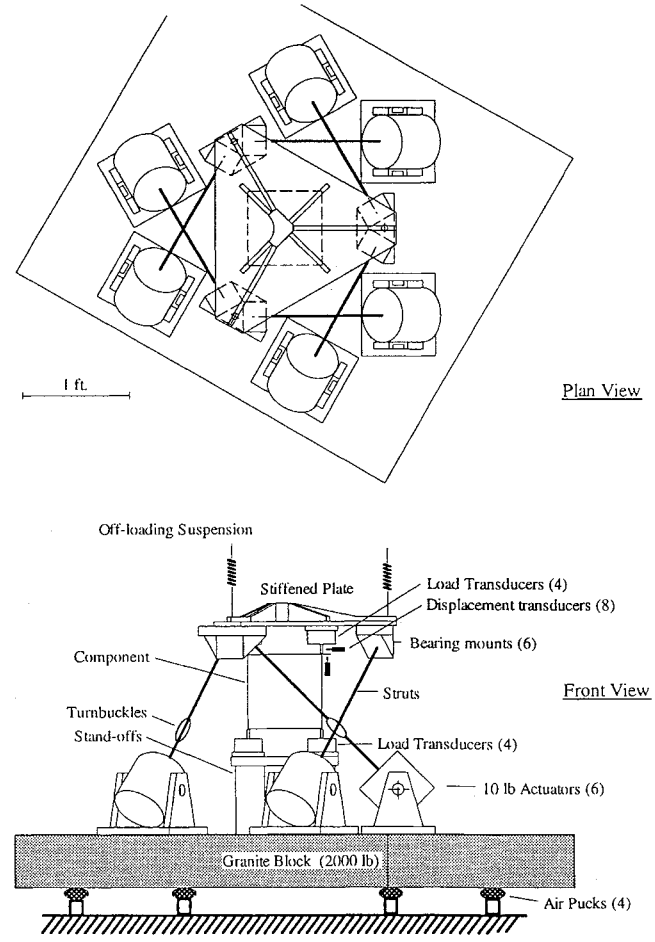

Fig. 3 Plan and elevation of the MODE component tester.

maintaining stiffness in the load path. This assures that the load application is determinate. The weight of the stiffened plate, the top sensors, and support struts is off-loaded through an axial suspension system. The component to be tested is mounted between the granite base and the stiffened plate using standoffs, which provide for coarse position adjustment. Built-in strut turnbuckles are used for fine positioning and fit adjustment.

The load and stroke requirements drove the actuator choice and geometrical arrangement of the tester. The requirements for generalized load capacity called for 100-in.lb maximum moments transmitted by the stiffened plate to the test article, and maximum shear loads of 20 lb. The stroke requirements dictated a maximum linear actuator stroke of approximately 0.070 in. Six Bruel & Kjaer 10 lb, ± 0.150-in. stroke, linear electromechanical actuators coupled through the geometry of the Stuart platform yielded the required stroke and loads. The resulting loads which can be applied to the test article by the top plate are 40-lb force in the axial direction, 34 lb in shear, and 140 in.lb of moment. The maximum stoke achieved with no test specimen mounted is approximately 0.080 in. and ± 0.01 rad.

The sensors used include force and displacement sensors. The required displacement measurement range and resolution for the MODE components are 0.020 in. and 0.00005 in. respectively. The deflections of the top nodes of the MODE bay were measured with inductive bridge Kaman noncontacting sensors. The velocities were estimated for a discrete data time window using the discrete fourier transform pair $\dot{x} \Leftrightarrow j\omega X(\omega)$. It was assumed that the lower nodes, attached to the granite block, were fixed. The load cell measurement range and resolution for the MODE components are 50 lb, 150 in.lb, 0.1 lb and 0.3 in.lb, respectively. Transmitted forces at the top and bottom of the bay were measured with JR^3 multiaxial load cells. In theory, the six generalized displacements and reactions of the top frame of the bay can be inferred from six displacement sensors and six axes of force measurement. In practice, the practical constraints of load size, component geometry, and measurement accuracy require the use of eight displacement sensors and four three-axis load cells. The six DOF information is obtained by averaging the excess information from these measurements. It should be emphasized that great care was taken to make exactly collocated and collinear force and displacement measurements.

Data on two test articles are presented in this paper. The component tester was first calibrated with a simple, nominally linear, truss bay. The longerons, diagonals, and battens are 3/8-in.-diam solid lexan rods, which are epoxied into 1.25 × 1.25-in. aluminum nodes. The calibration bay compliance was chosen so as to approximate the high preload MODE deployable bay.

The second test article is one deployable bay of the MODE STA. This particular deployable bay incorporates a mechanism for varying the pretension on the diagonal bracing wires allowing three possible tension settings of approximately 7, 13, and 27 lb (Ref. 7). Identification of this bay is presented for the high and low levels of pretension with the inference that the medium preload shows no new information.

Procedure

The actual experimental procedure includes setup, excitation, data aquisition, and processing. Great care was taken to mount each test component with minimal deformation and preload induced by the test rig. Both force and displacement sensors are used in the setup process to indicate adverse loading on the component.

Inputs are commanded to the component tester as time history voltages to the shakers. These are programmed in an experiment control computer and down loaded to a digital-to-analog (D/A) device, the outputs from which are smoothed before being amplified and passed to the actuators.

Logical choices of test input directions are the set which decouples the measured transmitted force or the set which decouples the measured displacements. These directions are determined by a process of calibration of the component mounted in the component tester. An initial guess is made of the set of actuator inputs which will achieve the desired directions. The initial guess can be made using the geometry of the tester, a finite element model of the component, and assuming perfect actuators. Test data are then taken, and the next estimates of best commands to the actuators are computed using a preliminary linear least squares fit of the data. Iterating usually results in the desired directions.

Tests are performed in the now-determined individual directions so that dominant input directions can be distinguished. Eight channels of displacement data and 24 channels of force data are stored in a Camac crate, after prefiltering at the Nyquist frequency using programmable analog filters. Filters in the force and displacement sensor conditioning were removed so that all channels are passed through the programmable filters with nominally the same filter gain and lag characteristics. The data are up loaded to the control computer after each test.

Numerical algorithms are then used to compute the collocated six DOF measurement time histories from the data. Velocity state estimation is made using full reconstruction of the time history via the Fourier transform pair. The data are now available for component identification described earlier.

Experimental Results

Calibration Bay

In this section, identification results are presented on the calibration and MODE deployable bay. The calibration identification results are presented as proof of concept, experiment, and as justification for assumptions made while testing the MODE bay. In both cases, the parameter enumeration is with reference to the physical vectors

$$f_T = [f_x \quad f_y \quad f_z \quad M_x \quad M_y \quad M_z]^T$$
$$x = [u_x \quad u_y \quad u_z \quad \theta_x \quad \theta_y \quad \theta_z]^T \tag{18}$$

where the subscripts x and y denote directions that lie in the batten frame (cross section) of the bay components, and the z subscript denotes the direction longitudinal through the bay.

Table 1 lists the results of the identification of the 6 × 6 compliance matrix for the calibration bay for three sets of directions and three frequencies. A sample of the dominant elements of the compliance matrix (i.e., the nominally nonzero entries) are listed. The diagonal terms are listed first, followed by the coupling terms. The compliances have been normalized to the units meter/newton for comparison purposes (moments and angles have been normalized by $l = 0.2$ m). Comparison of a finite element model (FEM) with extended least squares and iterative least squares methods is made as an indication of the accuracy of the data. The precision of the identification process is indicated by the standard deviations returned by static least squares analysis. Consistency of the identification is checked by comparing those parameters which, by the FEM, should be nominally equal. No attempt has been made to enforce symmetry on the matrix during the identification process.

The finite element model, typical of nonupdated first generation models, was constructed with handbook material data and geometrical measurement. Comparison of the FEM with the extended least squares and iterative least squares identification shows an average discrepancy 6% for the diagonal terms and 10% for the off-diagonal terms. It is difficult to determine whether these discrepancies reflect on the absolute accuracy of the FEM or identified data. If this degree of inaccuracy were attributed to the finite element model, it would correspond to a 3–5% error in predicted frequency, which is well within the range of accuracy expected for a first generation FEM.[5]

Precision of the measurements is indicated in Table 1 as the parameter standard deviation given as a percentage of the identified parameter. The torsion compliance $C_{(6,6)}$ has the lowest standard deviation, which is approximately 2%. It is not surprising that the torsion term is identified with lowest standard deviation since it is the most compliant direction identified and, therefore, the signal to noise ratio is high. For the same input directions, the parameter standard deviation increases with decreased compliance. For example, the axial compliance has a standard deviation of 13% for the 1-Hz, orthogonal force case.

Consistency is indicated by examining the pairs of compliance parameters that should ideally be the same (as indicated by the finite element model). Good consistency is indicated in the diagonal shear terms, $[C(1, 1)$ vs $C(2, 2)]$ and the bending terms

Table 1 Six DOF compliance identification of the calibration bay

Compliance parameter $\times 10^{-5}$ m/N	FEM	Linear extended least squares fit										Iter. LSQ
		$\perp F$, 1 Hz		$\perp x$, 1 Hz		rand., 1 Hz		$\perp F$, 5 Hz		$\perp F$, 15 Hz		$\perp F$, 1 Hz
	C	C	σ_C, %	C	σ_C, %	C	σ_C, %	C	σ_C, %	C	σ_C, %	C
$C(1,1)$	0.269	0.266	4	0.277	4	0.270	13	0.266	5	0.276	3	0.264
$C(2,2)$	0.269	0.256	3	0.264	3	0.251	6	0.256	4	0.269	3	0.255
$C(3,3)$	0.033	0.034	13	0.036	20	0.035	18	0.034	17	0.035	19	0.035
$C(4,4)$	0.126	0.139	7	0.141	5	0.137	34	0.138	9	0.142	9	0.140
$C(5,5)$	0.126	0.138	5	0.142	8	0.142	56	0.138	7	0.142	7	0.139
$C(6,6)$	0.583	0.536	2	0.552	2	0.548	2	0.537	2	0.563	1	0.534
$C(1,4)$	0.061	0.071	14	0.072	11	0.068	75	0.071	18	0.076	18	0.074
$C(4,1)$	0.061	0.069	13	0.071	13	0.068	46	0.070	16	0.073	10	0.072
$C(1,5)$	0.064	0.072	11	0.076	16	0.069	123	0.072	14	0.078	14	0.072
$C(5,1)$	0.064	0.067	13	0.068	14	0.068	47	0.067	17	0.069	10	0.067

Table 2 Six DOF stiffness identification of the MODE bay in SI units (units omitted for clarity)

Elements	Parameters					
F_{ij}	K_1	K_2	K_3	D_1	F_s	K_b
Low Preload						
F_{11}	1.471×10^5	-8.894×10^7	-1.008×10^{12}	1.121×10^2	1.586×10^0	6.201×10^4
F_{22}	1.607×10^5	-1.729×10^7	-1.157×10^{12}	1.193×10^2	1.292×10^0	6.219×10^4
F_{33}	5.405×10^6	-1.181×10^{10}	-2.046×10^{15}	2.066×10^3	no fit	no fit
F_{44}	4.965×10^4	1.780×10^6	-1.114×10^{11}	2.290×10^1	0.412×10^0	6.908×10^3
F_{55}	4.840×10^4	-1.039×10^7	-8.823×10^{10}	2.209×10^1	0.525×10^0	7.775×10^3
F_{66}	3.023×10^3	-1.799×10^4	-1.205×10^8	2.269×10^0	0.338×10^0	1.352×10^3
F_{15}	-2.450×10^4	-6.527×10^6	-8.539×10^{10}	-6.351×10^0	no fit	no fit
F_{51}	-1.880×10^4	1.295×10^6	2.225×10^{10}	-3.939×10^1	no fit	no fit
F_{24}	2.646×10^4	-1.433×10^6	-4.456×10^{10}	1.438×10^1	no fit	no fit
F_{42}	2.064×10^4	-4.733×10^6	-3.148×10^{11}	4.465×10^1	no fit	no fit
Med. Preload						
F_{11}	2.941×10^5	2.354×10^7	-1.072×10^{10}	1.200×10^2	1.964×10^0	4.861×10^4
F_{22}	2.957×10^5	7.322×10^7	-2.983×10^{12}	1.191×10^2	1.466×10^0	3.729×10^4
F_{33}	5.826×10^6	-1.936×10^9	-2.152×10^{15}	2.050×10^3	no fit	no fit
F_{44}	5.418×10^4	4.985×10^6	3.858×10^{10}	1.798×10^1	0.460×10^0	7.250×10^3
F_{55}	5.588×10^4	-7.622×10^5	-7.523×10^9	1.958×10^1	0.365×10^0	5.569×10^3
F_{66}	5.503×10^3	4.400×10^4	-7.954×10^7	3.035×10^0	0.665×10^0	1.237×10^3
F_{15}	-4.074×10^4	-6.565×10^6	2.260×10^9	-9.494×10^0	no fit	no fit
F_{51}	-3.638×10^4	-5.787×10^6	2.606×10^{11}	-3.736×10^1	no fit	no fit
F_{24}	3.912×10^4	4.271×10^6	9.457×10^8	9.673×10^0	no fit	no fit
F_{42}	3.552×10^4	1.088×10^7	-2.362×10^{11}	2.918×10^1	no fit	no fit
High Preload						
F_{11}	3.683×10^5	5.314×10^6	-4.891×10^{11}	5.437×10^1	0.332×10^0	9.359×10^3
F_{22}	3.724×10^5	1.175×10^7	-1.469×10^{11}	3.250×10^1	0.227×10^0	7.359×10^3
F_{33}	6.140×10^6	-1.509×10^{10}	-1.687×10^{15}	9.861×10^2	no fit	no fit
F_{44}	6.538×10^4	1.390×10^7	-1.323×10^{11}	1.585×10^1	no fit	no fit
F_{55}	6.529×10^4	8.922×10^5	-7.812×10^{10}	1.502×10^1	no fit	no fit
F_{66}	7.150×10^3	4.717×10^4	-3.007×10^7	1.106×10^0	0.244×10^0	4.467×10^2
F_{15}	-4.662×10^4	-4.852×10^6	2.348×10^{10}	-4.429×10^0	no fit	no fit
F_{51}	-4.281×10^4	1.480×10^6	2.236×10^{11}	-1.315×10^1	no fit	no fit
F_{24}	4.571×10^4	1.132×10^7	-8.405×10^{10}	2.030×10^0	no fit	no fit
F_{42}	4.244×10^4	-9.976×10^4	-3.431×10^{11}	8.000×10^0	no fit	no fit

[$C(4,4)$ vs $C(5,5)$], although more deviation is evident in the off-diagonal terms; e.g. [$C(1,4)$ vs $C(4,1)$]. The shear compliances differ by approximately 4% whereas the bending compliances differ by less than 1%. The off diagonals differ by 5% on average.

Three sets of directions tested were as follows: orthogonal generalized forcing ($\perp F$); orthogonal generalized displacement ($\perp x$), i.e., the set of forces which best decoupled the displacement outputs; and a randomly selected set of forces (rand.). Each set were normalized to have approximately the same input energy. The reported parameter σ_C, developed in Eqs. (13–17), shows that for a diagonally dominant test article there is little difference between orthogonal generalized forcing and orthogonal generalized displacements and random inputs generally produce poorer results. The randomly chosen set of directions in this experiment does not adequately span the input force space. The choice of either orthogonal generalized forcing or orthogonal generalized displacements is strongly influenced by the sensor noise e_x as shown in Eqs. (13) and (17). For the data presented in this paper, the noise floor is determined by the A/D converter independent of the physical sensors and, therefore, it is not surprising that neither of these two options is clearly superior.

Identification at the three test frequencies with orthogonal force sets showed no significant change in the standard deviation of the identified parameters. The compliance of the 1- and 5-Hz data is nearly identical whereas the 15-Hz data showed approximately uniform softening of 4% when compared to the 1-Hz data. This trend indicates the increasing importance of the inertia terms (for which the data have not been corrected) as the frequency increases. For the calibration bay, the quasistatic assumption produced an estimated 1% error due to inertia terms at 10 Hz. Both the data and this estimate therefore support the quasistatic assumption in the 0–10-Hz test frequency range.

Comparison of extended least squares and iterative least squares methods show agreement within 2% in the diagonal terms and 3% in the off-diagonal terms. This is due to the different treatment of cost in the respective methods.

In summary, the results of the calibration bay indicate acceptable accuracy, precision, and consistency as well as a preference for orthogonal generalized displacement or force input; and they support the quasistatic testing and nonlinear least squares parameter identification.

Mid-Deck 0-Gravity Experiment Deployable Bay

Data presented on the MODE deployable bay were taken at 7.5 Hz for high, medium, and low wire pretensions (joint preloads) and with inputs that decoupled the displacements. In Figs. 4–6 and 8, the transmitted force (shown for each of the diagonal DOF x_i) is the relevant measured force f_{T_i} minus the contributions from nondiagonal degrees of freedom,

$$\begin{aligned} f_y &- (F_{2j})_{j\neq 1} \\ M_y &- (F_{5j})_{j\neq 5} \\ M_z &- (F_{6j})_{j\neq 6} \end{aligned} \tag{19}$$

High preload data load stroke plots are shown in the upper row of Fig. 4 for typical diagonal DOF. The plots show that the bay stiffness at high preloads is dominantly linear. However, within the load-stroke information shown, sufficient nonlinearities exist to cause the softening and dampening phenomena witnessed in the ground and space modal tests.[7] Some hysteresis is evident in the θ_z and u_y directions. The θ_y data have been corrupted by A/D quantization error due to small rotations. Model fits to the data were performed using the nonlinear least squares continuation algorithm.

In the high preload case, only the shear and torsion F_{11}, F_{22}, and F_{66} were fit with the full model of Eq. (3), a cubic stiffness, a linear damping term, and the dynamic hysteresis model. The bending axes F_{44} and F_{55} were fit with a cubic stiffness and linear damping term, as were the nondiagonal F_{ij} models and the axial model F_{33}. The models are shown in the bottom row of Fig. 4. The dynamic hysteresis model clearly does a good job of modeling the hysteresis in the transmitted M_z and transmitted f_y. Models of the bending axes typically underpredicted what looks like damping in the θ_y data. However, the stiffness plot line width in the θ_y data is due to sufficiently random A/D noise and, therefore, the model returns low levels of dissipation.

Low preload data are shown in two different forms in Figs. 5 and 6. Figure 6 (upper row) shows the classic load stroke form of the diagonal transmitted forces, transmitted f_y, transmitted M_y, and transmitted M_z, in the u_y, θ_y, and θ_z direction tests, respectively. Force-state maps for all of the diagonal terms are shown in Fig. 5 with 90% of the identified linear stiffness contribution removed. The u_y and θ_z data show significant softening dynamic hysteresis consistent with Prandtl's laws. The θ_y data show some dynamic hysteresis at the low preload, which appears asymmetric. This could be a result of other coupled DOF influences not modeled by Eqs. (6) and (7). The axial data appear quite linear.

The nonlinear model in Eqs. (3) and (7), is fit to obtain the F_{11}, F_{22}, F_{44}, F_{55}, and F_{66} in Eq. (3). For this preload the nondiagonal F_{ij} of Eq. (4) were fit with a cubic backbone stiffness K_s and linear damping D_1 as was F_{33}.

Sample model fits are shown for the low preload cases in Fig. 6. The two parameter dynamic hysteresis model along with cubic stiffness and linear damping appears to do a good job of fitting the multidimensional data. Error surfaces are shown for a sample of the low preload diagonal terms in Fig. 8. Each surface is the data transmitted force minus the fit model transmitted force as a percentage of the maximum linear restoring force in that DOF [Eq. (20)].

$$e_i = \frac{f_{T_i} - F_{T_i}}{K_{1_i} x_{i_{\max}}} \tag{20}$$

The surfaces show error within several percent. Higher order analytic dependencies, which can be seen in the error surfaces, are used as an indicator of nonmodeling during the modeling and identification process.

The implication from such a good fit of the dynamic hysteresis model to the hysteresis (shown in Fig. 6) is that the joints dominate the structural behavior at low preloads. The fits support the fact that the mechanism has been identified and that the hysteresis also appears in the θ_y and θ_x data for low joint preloads.

Further evidence of the joint friction is seen in Fig. 7. In this experiment, the diagonal bracing wires were completely removed

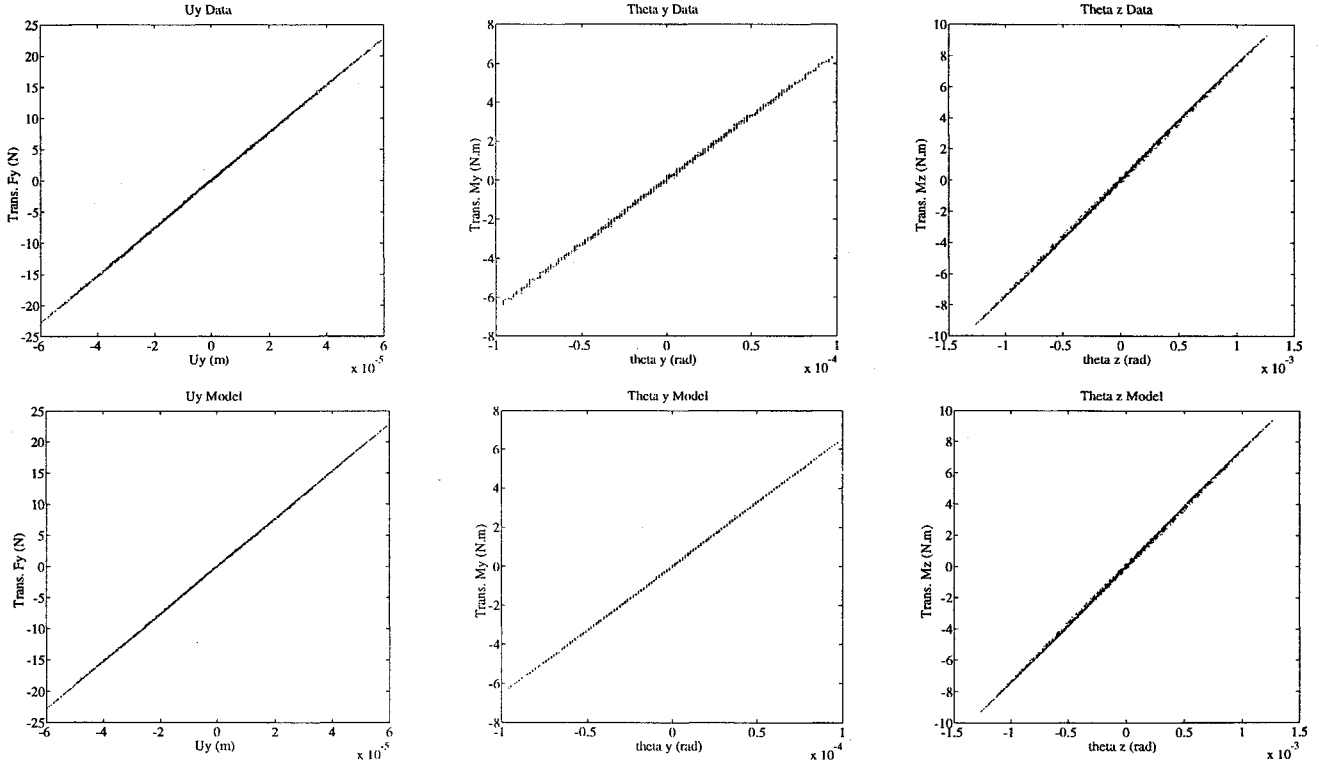

Fig. 4 High joint preload MODE bay data (upper row) and nonlinear function fits (lower row) for the u_y, θ_y, and θ_z input directions.

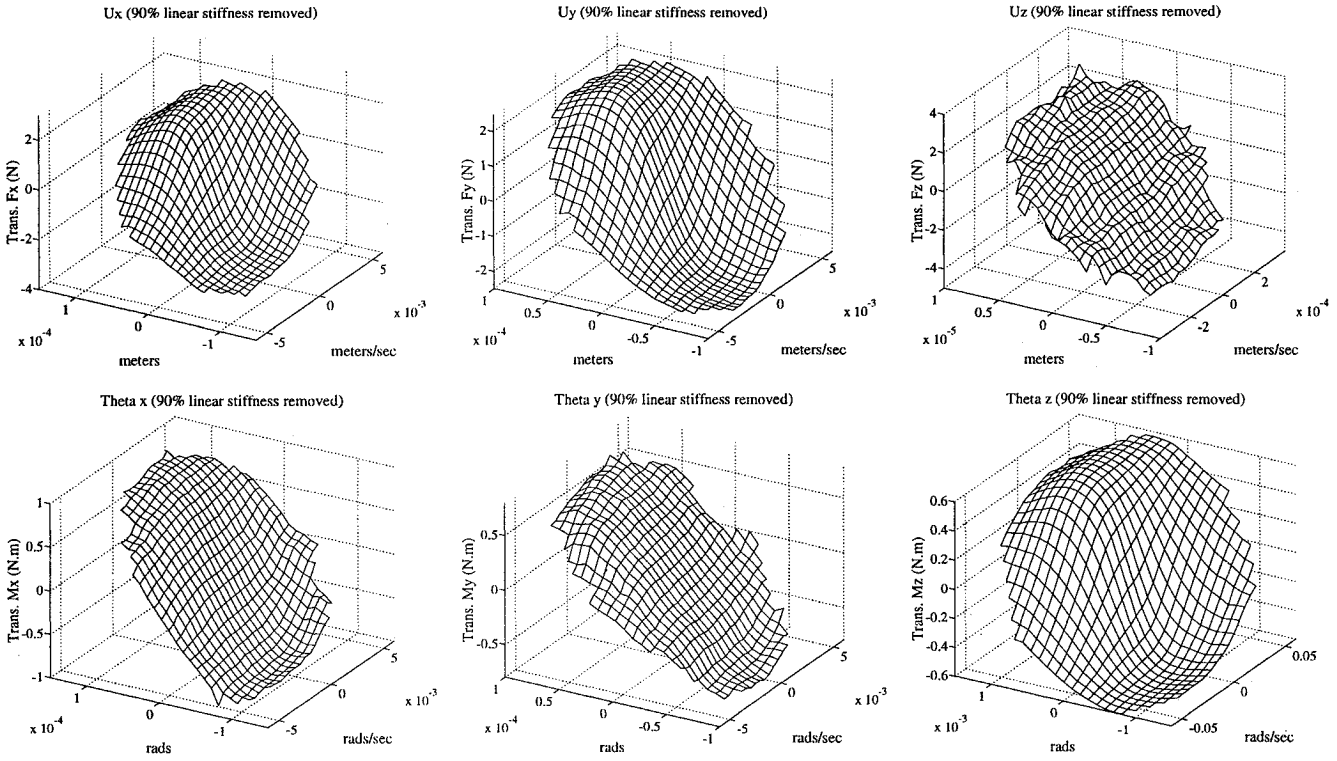

Fig. 5 Low joint preload MODE bay data force-state maps.

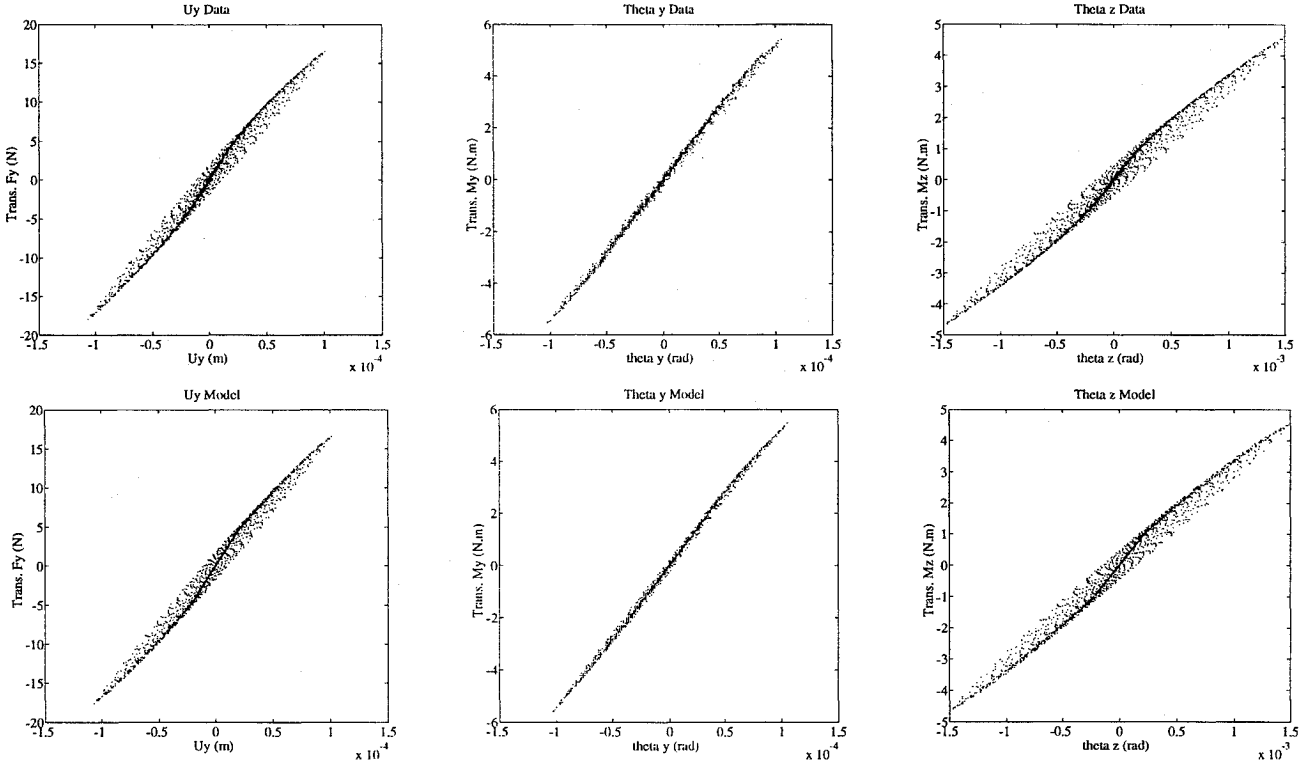

Fig. 6 Low joint preload MODE bay data (upper row) and nonlinear models (lower row) for u_y, θ_y, and θ_z input directions.

from the bay so that the joint mechanism could be isolated and identified. The mechanism also included a set screw which could lock the pin joint rigidly and thus eliminate any rotation at the pin joint.

The data shown in Fig. 7 are for standard pinned joints vs joints locked by set screw. In the torsion test all pins were locked. In the shear test the four pins with rotation axis orthogonal to the forcing direction were locked and the four others were left free. The data of Fig. 7 show that the stiffness measured with the joints locked is identical to the low amplitude stiffness when the joints are free. With the joints unlocked, strong hysteresis is present, where as with the joints locked, virtually no hysteresis is present. Thus the low amplitude stiffness is consistent with the locked stiffness, and the high amplitude hysteresis is consistent with Prandtl's laws. Therefore, there is a strong indication that the softening and dampening observed in the MODE modal data is due to joints microslipping.

The fit parameter results are listed in Table 1. The units of the diagonal entries of Table 1 are in newton/meter and newton.meter/rad, respectively, and newton/rad and newton.meter/meter, respectively,

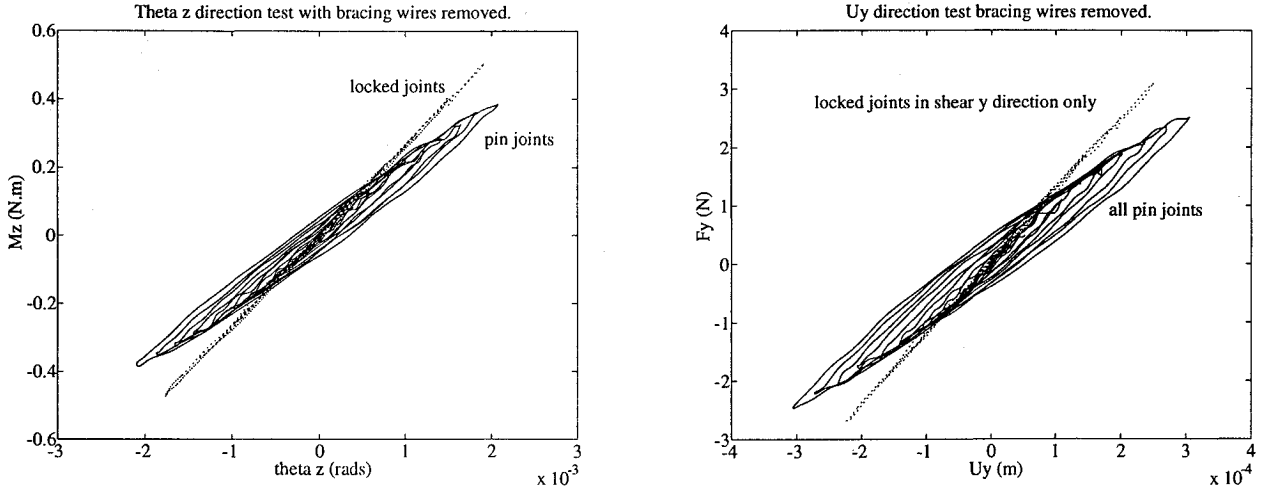

Fig. 7 Measured data for MODE bay with locked and free joints, bracing wires removed.

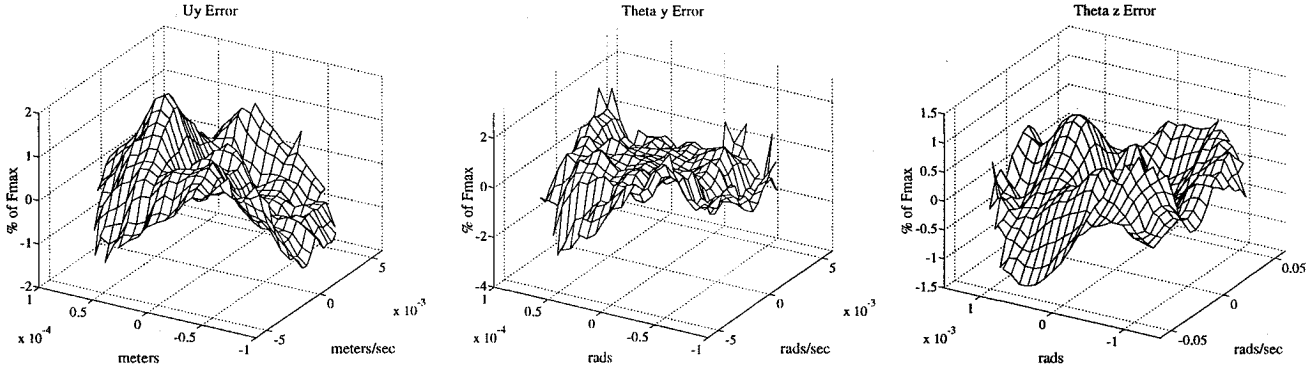

Fig. 8 MODE bay model fit error of diagonal functions F_{ii}.

for the linear coupled stiffness terms. The units of the nonlinear stiffnesses and linear damping terms are in their respective Standard International units. The diagonal functions F_{ii} are listed first. These are followed by the dominant coupling functions F_{ij}. For clarity, as with the calibration bay, no attempt was made to constrain the elemental fit to be symmetric.

Comparing the nominally identical linear shear stiffness terms for F_{11} and F_{22} with each other in each of the high, medium, and low preload cases, and normalizing with respect to their average, yields 1%, 0.5%, and 6% differences. Comparing the linear bending terms F_{44} and F_{55} in a similar fashion yields 0.1%, 3%, and 2.5%, respectively. For reference, the F_{15} and F_{51} linear terms compare with 8%, 11%, and 26%. This trend shows that as the joint preload decreases, the nominally similar directions become less consistent. In practice, the cables are not ideally preloaded to equal tension, and their pretension strongly effects the bay stiffness as a component.

The fit parameters show softening in the linear stiffness parameters of up to 60% when high and low joint preloads are compared. This shows that the bracing wires contribute strongly to the overall stiffness of the bay.

The nonlinear terms in Table 1 (K_{2_i} and K_{3_i}) show the increased importance of the higher order analytic stiffness at low preloads. The low joint preload diagonal terms show that the cubic stiffness contributions to the transmitted force increase as a percentage of the linear stiffness contribution, as is shown by Fig. 6. The quadratic stiffness force contribution $K_{2_i}x_i^2$ increases as the preload decreases for the F_{11}, F_{22}, and F_{66} fits. Quadratic dependencies can result from cable slackening phenomenon which is more likely at low joint preloads and was visualized during the low and medium joint preload experiments. Note that the quadratic and cubic dependencies are not the dominant nonlinearities of the component.

The linear damping term D_1 is consistent in the diagonal elements when comparing low and medium preloads for all six diagonal functions. In the high preload case, the D_1 parameter drops by approximately 50%.

The dynamic hysteresis model parameters F_s and K_b, are consistent, within reason, and show strong dependencies on the joint preload. The low amplitude stiffness difference K_b softens with increasing preload. This is shown in the high and low preload load stroke plots (Figs. 4 and 6). With increased preload, the low and high amplitude stiffnesses become comparable and, therefore, their difference K_b should soften. The slip force parameter F_s drops significantly in the high preload case with respect to the low and medium preloads. This physically indicates the decrease in joint participation as the preload restrains the joint mechanism. This is a similar effect to that shown in Fig. 7.

Conclusions

The force-state mapping approach was successfully extended to the characterization of a multidegree-of-freedom system with memory effects. A general constitutive relation between quasistatic transmitted force and mechanical state was developed, which distinguishes rate dependent effects from true memory effects, and diagonal effects from coupling terms. The model was then specialized for deployable truss structures, by including up to cubic stiffness analytic terms plus a term capturing dynamic hysteresis effects. The two parameter dynamic hysteresis model is representative of microslipping of the dozens of frictional interfaces at the pins of a deployable truss and is consistent with Prandtl's postulated laws.

A device was constructed which allows controllable independent inputs of six axes of generalized load, measurements of six generalized forces at each end of a cantilevered test bay, and measurements of six generalized displacements at the unconstrained end. Computer control of the inputs allowed arbitrary time history and spatial direction of the unsteady force, in the presence of a potentially nonzero arbitrary steady preload.

An identification algorithm was developed which first uses extended least squares to identify linear parameters and their covariance. Using the linear fit as a starting point, a nonlinear fit procedure first fits the diagonal terms and then, using a continuation approach, allows off-diagonal influences to be determined while updating the diagonal terms.

The identified parameters for an nominally linear elastic reference bay provide a good check of internal consistency, accuracy, and precision. The data are internally consistent, in that diagonal terms which should be similar are similar, as are off-diagonal terms which should be symmetric. The variance of the parameters indicates a precision of several percent, and maximum precision is obtained by forcing in a principal direction of the linear stiffness matrix. The accuracy of the parameters is good, considering that the reference (a first generation model) is not expected to have model accuracy better than 5%. The nonlinear parameter fit returned linear parameters quite close to the linear procedure for the nominally linear calibration bay.

The identified parameters for the deployable MODE bay are internally consistent and are in general agreement with the trends observed in the modal testing. In particular, the dynamic hysteresis model fits the data quite well and predicts the dampening and softening observed in the torsion and shear modes of the MODE STA. The physical origin of this dynamic hysteresis is the frictional sliding of the pins in the longerons. This model also correlates with the lack of softening in the bending modes, where relative motions of the pin joints are small.

Acknowledgments

This work was supported by the NASA Instep Flight Experiments Program, and the NASA Langley Research Center Reference NAS1-18690, with Sherwin Beck as monitor; and by the NASA Headquarters Grant NAGW-1335 to the MIT Space Engineering Research Center, with Robert Hayduk as technical monitor. The authors also wish to thank Marthinus van Schoor for his many contributions to the development of the MODE component tester.

References

[1]Crawley, E. F., and O'Donnell, K. J., "Force-State Mapping Identification of Nonlinear Joints," *AIAA Journal*, Vol. 25, No. 7, 1987, pp. 1003–1010.

[2]Crawley, E. F., and Aubert, A. C., "Identification of Nonlinear Structural Elements by Force-State Mapping," *AIAA Journal*, Vol. 24, No. 1, 1986, pp. 155–162.

[3]Pinson, L. D., and Hanks, B. R., "Large Space Structures Raise Testing Challenges." *Astronautics and Aeronautics,* Vol. 21, No. 10, 1983, p. 34.

[4]Press, W. H., Flannery, B. P., Teukolsky, S. A., and Vetterling, W. T., *Numerical Recipes—The Art of Scientific Computing,* Cambridge Univ. Press, 1986.

[5]Crawley, E. F., Barlow, M. S., and van Schoor, M. C., "Variation in the Modal Parameters of Space Structures." AIAA/ASME/ASCE/AHS/ASC 33rd Structures, Structural Dynamics and Materials Conference, 1992.

[6]Crawley, E. F., Barlow, M. S., van Schoor, M. C., and Masters, B. P., "Zero Gravity Measurement of the Modal Parameters of Space Structures." American Society of Mechanical Engineers Winter Annual Meeting, Nov. 1992.

[7]Crawley, E. F., van Schoor, M. C., and Bokhour, E. B., "The Middeck 0-Gravity Dynamics Experiment," NASA Contractor Rep. 4500, March 1993.

[8]Felippa, C. A., and Park, K. C., "Direct Time Integration Methods In Nonlinear Structural Dynamics," *Journal of Applied Mechanics*, Vol. 45, Sept. 1978, pp. 595–602.

[9]Craig, R. R., "A Review of Time-Domain and Frequency Domain Component Mode Synthesis," *International Journal of Analytical and Experimental Modal Analysis*, Vol. 2, No. 2, 1987, pp. 39–72.

[10]Rey, D. A., Crawley, E. F., Alexander, H., Glaese, R. M., and Gaudenzi, P., "Gravity and Suspension Effects on the Dynamics of Controlled Structures," Structural Dynamics and Materials Conference, AIAA Paper 93-1662, 1993.

[11]Kienholz, D. A., Crawley, E. F., and Harvey, T. J., "Very Low Frequency Suspension Systems for Dynamic Testing." AIAA Paper 89-1194, 1989.

[12]Chapman, J. M., Shaw, F. H., and Russell, W. C., "Nonlinear Transient Analysis of Joint Dominated Structures," AIAA Paper 87-0892, 1987.

[13]Dahl, R. P., and Wilder, R., "Math Model of Hysteresis in Piezo-Electric Actuators for Precision Pointing Systems," *Advances in the Astronautical Sciences*, Vol. 57, Paper AAS-011.

[14]Prandtl, L., "Ein Gedankenmodell zur kinetischen Theorie der fasten Korper," *Zeitschrift fur angewandte Mathematik und Mechanik*, Vol. 8, 1928, pp. 85–106.